Rock Mech Rock Eng (2014) 47:1939–1950
DOI 10.1007/s00603-013-0457-9

TECHNICAL NOTE

Observation and Numerical Analysis of the Scope of Fractured Zones Around Gateroads Under Longwall Influence

Qing-Sheng Bai · Shi-Hao Tu · Fang-Tian Wang · Xiao-Gang Zhang · Hong-Sheng Tu · Yong Yuan

Received: 11 May 2013 / Accepted: 12 July 2013 / Published online: 25 July 2013

Keywords Field observation · Numerical modeling · Scope of fractured zones (SFZ) · Gateroad · Longwall gob simulation

1 Introduction

There exists a trend in China that high productivity longwall face which produces 8.0–10.0 million tons of raw coal per annum is widely employed. The stability of the gateroads during the life of longwall mining is the main concern of the success of high-production longwall face. After a gateroad is driven into rock strata, the primary equilibrium state is disturbed and, as a result, the surrounding rocks are unavoidably broken or fractured (Dong et al. 1994). The extent of the fractured zones mainly depends on: stress characteristics where the gateroad is located; physical, mechanical and rheological properties of rocks; tectonic structure of the rock mass; and an applied extraction and support system (Cai 2008; Chu et al. 2007; Coggan et al. 2012; Feng et al. 2012; Wang et al. 2000). In the case of longwall gateroads, the SFZ can rapidly develop with the influence of longwall mining (Esterhuizen and Barczak 2006; Hao et al. 2004; Walentek et al. 2009). Accurately evaluating the SFZ under the influence of excavation and longwall mining is an important issue for support design and gateroad maintenance.

Q.-S. Bai · S.-H. Tu (✉) · F.-T. Wang · X.-G. Zhang · H.-S. Tu · Y. Yuan
Key Laboratory of Deep Coal Resource, Ministry of Education of China, School of Mines, China University of Mining and Technology, Xuzhou 221116, Jiangsu, China
e-mail: papertsh@126.com

This technical note describes the observation results of fractured zones around gateroad surrounding rocks under a top-coal caving longwall influence. Numerical modeling was also employed in characterizing the failure zones around the gateroads.

2 Study Site

This technical note is based on the mining conditions of panel 14101 in the Majialiang coalmine, Shuozhou city, Shanxi province. The #4 coal seam is the current mining seam, which is buried 620 m deep, with an average thickness of 10.0 m and dip of 3°. A fully mechanized top-coal caving longwall face (Xie and Zhao 2009) is set up to excavate the #4 seam. In panel 14101, a 3.5 m high longwall face was operated at the floor of the coal seam, and top-slice coal with a thickness of 2.5–8.5 m was caved and produced through the windows behind shields. An adjacent longwall panel, namely 14102, was under development, as illustrated in Fig. 1.

Ventilation and access to the face were provided by two parallel pre-driven gateroads along each side of the panel. The rock part between gateroads B and C is the coal pillar, which is 20 m wide, as shown in Fig. 1. The gateroads are driven along the floor of the #4 seam with the width of 5.5 m and height of 3.9 m. The gateroads were reinforced by bolts and anchor cables in the roof, bolts in the solid abutment side, and fiberglass bolts in the working face side. Because of brittle failure occurring on the surface of gateroads, bolts and cables were enhanced with steel wire sheets and steel strips.

There is a 4.5–6.3 m thick mudstone layer with an average thickness of 5.0 m above the #4 seam, forming the immediate roof. The upper stratum is a strong 5.0 m thick layer constituted by gritstone and packsand. A layer of packstone with an average thickness of 2.5 m is right underneath the coal seam.

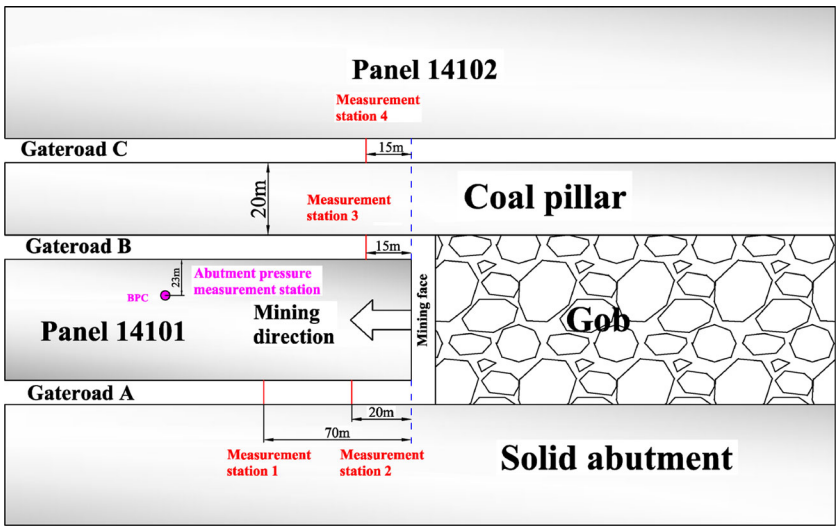

Fig. 1 Plan view of panel 14101

Under the packstone layer is a 2.5 m thick siltstone, a sand mudstone (5.0 m) and a 10.0 m thick bed of siltstone. The generalized stratigraphic column showing the coal seam together with the roof and floor strata is presented in Fig. 2.

3 In-Situ Measurements

A borehole press cell (BPC) was installed to measure the front abutment pressure as shown in Fig. 1. In order to determine the SFZ around gateroads, investigations using a borehole endoscope equipped with an infrared camera were implemented. Measurements were carried out in gateroads A, B and C with a distance of 15–70 m ahead of the longwall face. The measurement stations are illustrated in Fig. 1. Each measurement station had three boreholes in the roof, and one or two boreholes in the sidewalls with a length of 10–20 m and a diameter of 45 mm. One field observation was carried out in each measurement station. The layouts of prospecting holes in the measurement

Fig. 2 A generalized stratigraphic column at panel 14101

No.	Thickness (m)	Depth(m)	Formation
1	250	250	soil
2	140	390	Majority are mudstone and sand mudstone
3	120	510	Majority are fine and medium sandstone
4	70	580	Siltstone and packstone
5	15	595	Majority are mudstone
6	10	605	Siltstone
7	5	610	Mudstone and kaoline
8	5	615	Packstone
9	5	620	Mudstone
10	10	630	#4 coal
11	2.5	632.5	Packstone
12	2.5	635	Siltstone
13	5	640	Sand mudstone
14	10	650	Siltstone
15	16.5	666.5	Sandstone & mudstone
16	8.6	675.1	Packstone
17	12.3	687.4	Sand mudstone

stations and the fracture distribution are presented in detail in Fig. 3. The SFZ in the four measurement stations are listed in Table 1, and fracture densities (the number of fractures in every meter) in every hole were also counted.

As shown in Table 1, the SFZ in sidewalls (measured by boreholes 1-4 and 1-5) are 2–3 m larger than those in the roof (measured by boreholes 1-1, 1-2 and 1-3) in gateroad A, which is 70 m ahead of the longwall face. The fractures are dense around excavation boundaries, and sparse far from the gateroad. Because of the large distance from the active longwall face, the gateroad in measurement station 1 was not affected by the abutment loading. So it can be concluded that fractures around gateroad A in measurement station 1 are mainly a result of bulking of failed rocks, bedding planes and joints into the excavation. In measurement station 2, a distance of 20 m ahead of the active face, the SFZ and fracture densities increased compared with station 1. High abutment pressure around the station caused the discontinuities to rupture and rock blocks to move, consequently, fractures increased and spread. The SFZ increased by 1–2 m in the roof, but remained unchanged in sidewalls, as shown in Table 1. Compared with measurement station 1 and 2, borehole endoscope investigations in measurement station 3 (in gateroad B) and 4 (in gateroad C), demonstrated that fractures in the abutment peak area had developed to upper strata, as illustrated in Table 1; Fig. 3. Fractured zones in the roof vary in different places. The SFZ in the corner part is larger than the middle part, as the borehole 3-3 and 3-2 shown in Fig. 3c, and borehole 4-3 and 4-2 shown in Fig. 3d, but the difference of fracture densities in the boreholes within 12 m is unremarkable, as shown in Table 1.

Endoscopic tests indicated that fractures appeared along the whole borehole in borehole 3-3 and 4-3, and the SFZ in measurement stations 3 and 4 exceeded the length of testing boreholes. But the number of fractures in the two boreholes appearing in 10–20 m are much smaller than those in the first 10 m, as illustrated in Table 1; Fig. 3c, d. The fractures are relatively denser around the strata interface, as the boreholes 3-1, 3-2 and 3-3 shown in segment 5–7 and 10–11 m, and boreholes 4-1 and 4-2 shown in segment 10–11 m, which are emphasized with bold and italics numbers in Table 1. Boreholes 3-1 and 4-1, were chocked by fragments infilling and borehole dislocation, which implies that both rock dilation and shear movement between bedding planes occurred in the rock mass.

4 Numerical Simulations

Longwall mining disturbs the gateroad surrounding rocks in different ways; it varies with the distance from the mining face. Because of the stresses transferred, high pressure zones are created in the front of the face and its adjacent rock mass (Yavuz 2004). Mining induced stresses were simulated to assess the SFZ around the roadgates under longwall influence.

4.1 Longwall Gob Simulation

After extraction of the coal seam, the immediate roof in the mined area collapses and caves behind the working face. The gob compaction process has to be considered when modeling longwall mining. A hyperbolic equation after Ryder and Wagner (1978) was found to adequately represent the gob stress–strain behavior, which can be expressed as follows:

$$\sigma_{\mathrm{v}} = \frac{a \times \varepsilon_{\mathrm{v}}}{b - \varepsilon_{\mathrm{v}}}, \tag{1}$$

where a is a constant determining the gob's deformation modulus, b is the maximum vertical strain, and ε_{v} is the current vertical strain. a and b are empirically derived parameters, which are determined by model calibration and laboratory tests, as summarized in Table 2.

In Table 2, weak rocks represent the rocks that have a uniaxial compressive strength (UCS) of less than 40 MPa, like shales and claystones, while limestone, sandstones, and siltstones with UCS strength above 40 MPa could be classified as strong rocks.

As the gob consolidates, the stress increases. The cave-in material will be stiffer and the modulus will increase when the load increases. This strain-hardening material with irreversible compaction can be simulated using "double-yield" elements in FLAC3D (Itasca 2006). A FISH algorithm was established to regulate the gob response using Eq. (1).

4.2 Numerical Models Establishment

In accordance with the panels layout in Fig. 1, a FLAC3D model was established, and the model size is 486.5 × 300 × 140 m (length × width × height). The geometry of the model is sketched in Fig. 4a. The measurement stations are included in the model. The rock strata were modeled using Mohr–Coulomb strain softening (MCSS) elements, and the mechanical properties of the rock masses are presented in Table 3. The presence of bedding planes between strata, especially in mudstone beds, affects the overall shear resistance of a layer significantly. The mechanical properties of bedding planes are summarized in Table 3.

According to the field measurement data in Table 1, the SFZ is large, and the fractures are dense. To better capture the fractures around the gateroads, the element

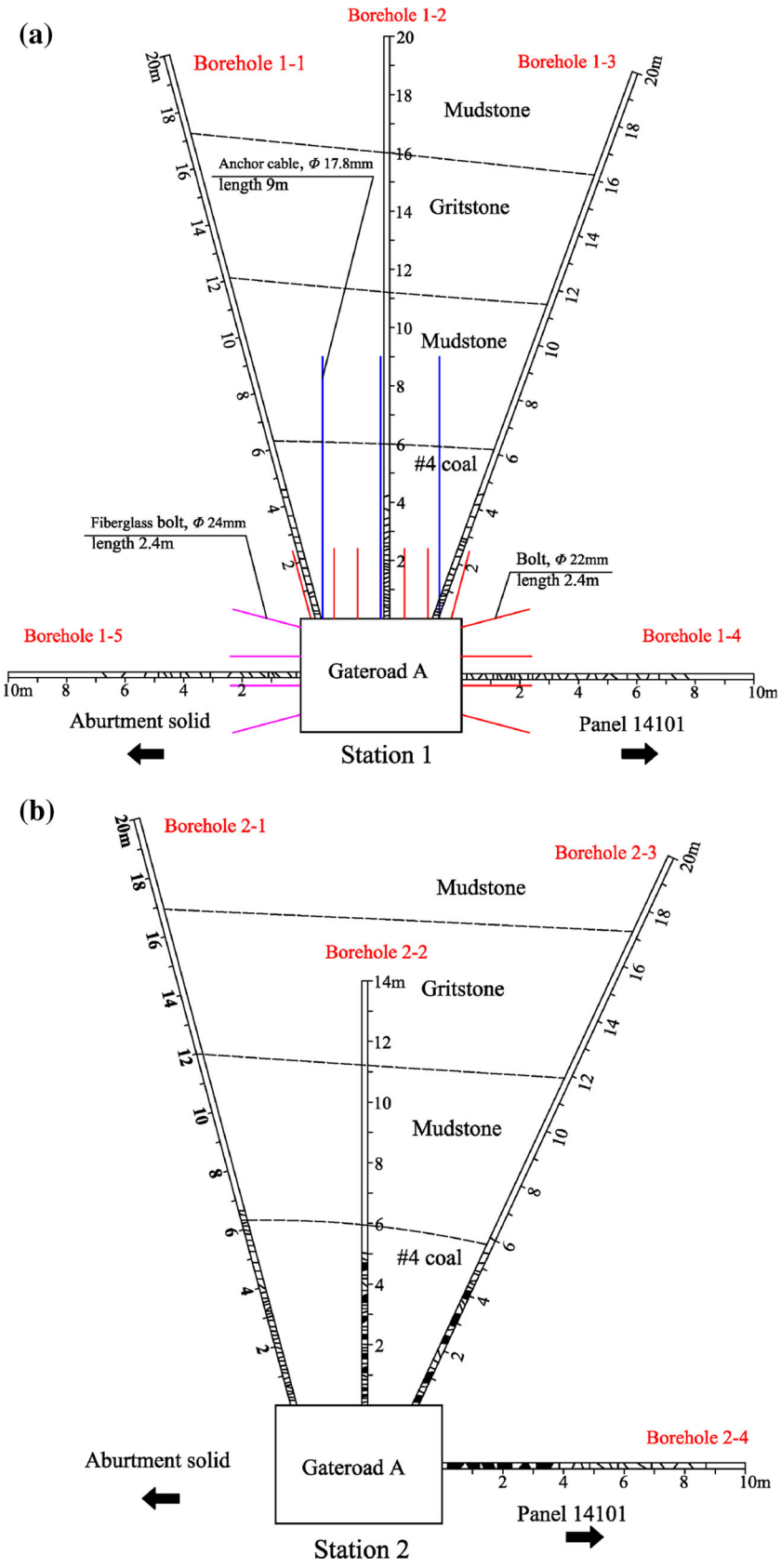

Fig. 3 Prospecting holes layouts and fracture distribution in the four measurement stations: **a** station 1, **b** station 2, **c** station 3, **d** station 4

Fig. 3 continued

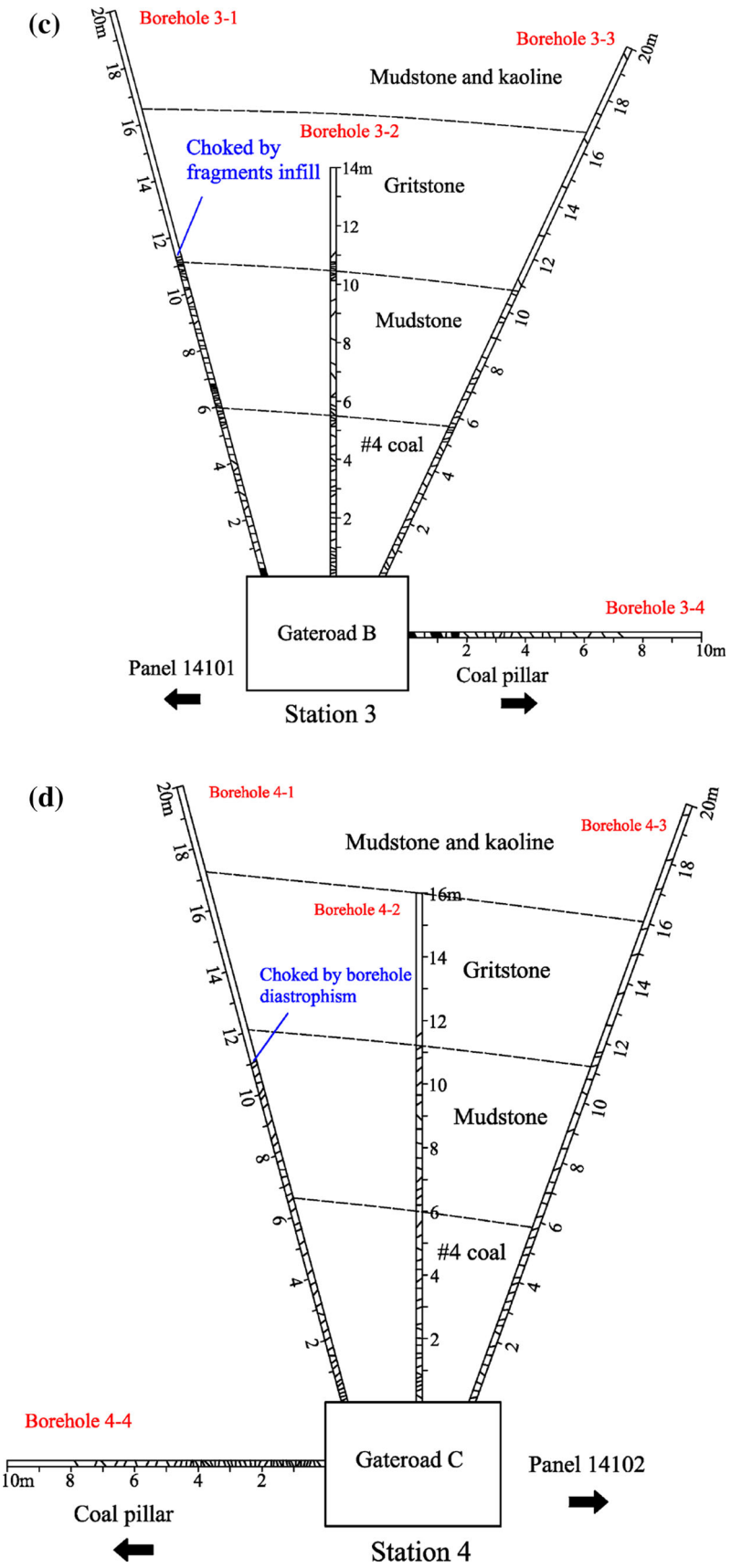

Table 1 The SFZ and fracture density in the observation boreholes

Measurement station name	Station 1					Station 2				Station 3				Station 4			
Distance from longwall face (m)	70					20				15				15			
Borehole name	1-1	1-2	1-3	1-4	1-5	2-1	2-2	2-3	2-4	3-1	3-2	3-3	3-4	4-1	4-2	4-3	4-4
SFZ (m)	4.58	4.2	4.6	6.6	7.8	6.6	5.0	6.1	8.7	[a]	11.1	19.9	7.1	[a]	11.6	19.6	7.9
Depth ranges along the boreholes (m)	Fracture densities																
[0, 1)	5	8	8	4	4	8	10	10	14	6	8	5	7	7	6	7	8
[1, 2)	3	7	5	6	4	7	12	7	10	3	4	4	7	5	5	3	9
[2, 3)	4	7	5	5	1	7	10	9	8	4	4	3	4	3	3	4	7
[3, 4)	2	4	2	4	3	7	9	8	6	4	5	3	4	3	3	3	8
[4, 5)	2	1	2	3	4	4	8	7	3	4	3	4	3	2	3	3	7
[5, 6)				2	1	5		3	3	**8**	**7**	**7**	2	3	2	3	3
[6, 7)				3	2	5			3	**12**	**3**	**3**	2	4	3	3	3
[7, 8)				2					2	4	1	3	1	3	3	2	2
[8, 9)									2	6	1	2		4	3	1	
[9, 10)										5	2	2		3	2	2	
[10, 11)										*8*	*7*	*4*		*4*	*3*	2	
[11, 12)										[a]	1	0		[a]	2	3	
[12, 13)												1				1	
[13, 14)												0				1	
[14, 15)												1				1	
[15, 16)												0				1	
[16, 17)												1				0	
[17, 18)												1				1	
[18, 19)												0				1	
[19, 20)												1				1	

Bold and italics values indicate relatively denser fractures around the strata interface

[a] Borehole was choked

Table 2 Parameters for modeling various gob types (Esterhuizen et al. 2010)

Overburden type	Ratio of strong:weak rocks (%)	*a* parameter (MPa)	*b* parameter
Weak	25	5.9	0.44
Moderate	35	8.6	0.44
Strong	50	12.8	0.44
Very strong	65	25.2	0.44

size should be less than 0.1 m around the gateroads. Large scale 3D models with massive elements are computationally intensive and require careful thought and implementation, and, thus, they are slow to compute (Hammah et al. 2009). A 2D model with fine elements can preferably express the failure process around the gateroads, and the computing time is also acceptable. Therefore, 2D models were used to simulate the fracture distribution around the gateroads. The 2D model was constructed in a vertical cross-section in the X–Z plane in the center of the 3D model where the field measurement stations were installed. The 2D models for station 1, station 2 and station 3 and 4 are established, respectively, which are shown in Fig. 4b, c. The boundary conditions of the 2D model are consistent with the 3D model except the upper boundary, where a distribution of the in-plane shear stress and vertical stress is applied. The applied stresses are determined in the 3D model and associated with the distance from the longwall face.

Numerical calculations for the gateroads were carried out using phase 2 (Rocscience 2012) based on FEM, assuming the rock mass is an elastic–plastic and isotropic medium according to the Hoek–Brown (1997) failure criterion. The physical and mechanical properties of the rock mass and discontinuities are identical with those in the 3D model (Table 3).

The gateroad surrounding rocks break gradually as the face approaches, and the strength of the failure rock becomes weaker compared with its initial state. In order to precisely estimate the deformation of the longwall gateroads, strength parameters would be modified appropriately when simulating the gateroad behaviors under the condition of post failure rock mass. Walentek et al. (2009) discovered the relations for determining the

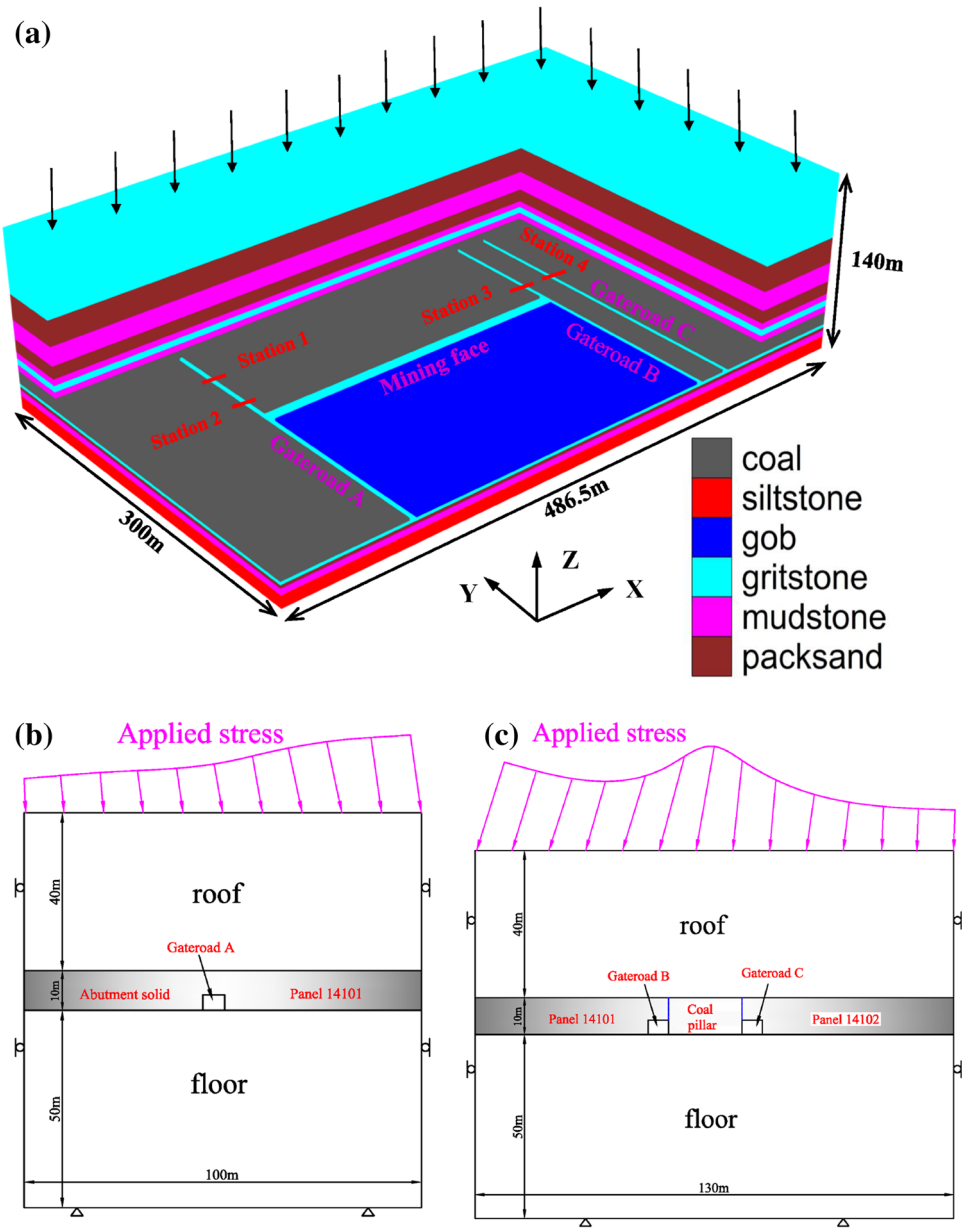

Fig. 4 **a** FLAC3D model, **b** 2D model for measurement station 1 and 2, **c** 2D model for measurement station 3 and 4

appropriate values of parameters m_b and s in the Hoek–Brown failure criterion for various rocks on the basis of extensive numerical calculations for longwall gateroads as well as statistical calculations. The relations are as follows:

$$m_{\mathrm{bp}} = c_1 \times \mathrm{e}^{c_2 \times d} \tag{2}$$

$$s_{\mathrm{p}} = c_3 \mathrm{e}^{c_4 \times d}, \tag{3}$$

where: d is the distance from the longwall face (positive values before and negative values behind the face), m. c_1, c_2, c_3 and c_4 are coefficients depending on strata lithology. Their values are presented in Table 4.

In Eqs. (2) and (3), the subscript "p" in m_{bp} and s_{p} denotes the post failure parameters.

Numerical simulations were performed to determine the rock mass failure zone around the longwall gateroads in the four stations, and the Hoek–Brown parameters m_b and s were properly modified. Supporting elements, bolt, anchor cable and fiberglass bolt were modeled in the form of "end anchored bolt" elements in phase 2 (Rocscience 2012).

4.3 Results of Numerical Modeling

Figure 5 shows the stress distribution gained from the numerical modeling and field measurements after panel 14101 passed the monitor site. It can be observed that the numerical model predicted a peak abutment stress of 42.2 MPa with a distance of 8.0 m in front of the face.

Table 3 Mechanical parameters of the rock mass and bedding planes

Rock type	γ (Kg/m^3)	K (GPa)	G (GPa)	C (MPa)	φ (deg.)	σ_t (MPa)	C_r (MPa)	φ_r (MPa)	e_p
Rock mass									
Coal	1,420	5.2	2.4	5.78	28	1.5	0.58	25	0.5
Mudstone	2,300	7.7	3.6	8.7	30	1.6	0.87	28	0.05
Gritstone	2,550	8.8	4.1	12.7	31	2.5	1.27	28	0.05
Packsand	2,600	9.5	6.2	13.5	32	3.2	1.35	29	0.05
Siltstone	2,650	8.2	4.3	9.5	34	2.4	0.95	30	0.05

Rock type	Cohesion (MPa)	Tensile strength (MPa)	Friction angle (°)
Bedding planes			
Mudstone	1.5	0.5	25
Gritstone	5.3	1.5	28
Siltstone	3.6	1.05	27
Packstone	2.1	0.8	28

γ is the unit weight, K is the bulk modulus, G the shear modulus, c the cohesion, φ the internal friction, σ_t the tensile strength, C_r the residual cohesion, φ_r the residual friction and e_p the plastic strain parameter at the residual strength

Table 4 Coefficients for determining post failure parameters m_b and s in the Hoek–Brown failure criterion (modified from (Walentek et al. 2009))

Strata lithology	Coefficients			
	c_1	c_2	c_3	c_4
Coal	0.627	0.0024	0.000494	0.00394
Clay shale	0.3197	0.0148	0.00041	0.01592
Sandy shale	0.5093	0.0127	0.000762	0.01881
Sandstone	0.7568	0.0127	0.001647	0.01697

These values were very close to those measurements from the BPC, which had a peak abutment stress of 43 MPa, 8.5 m ahead of the face.

The fracture and maximum shear strain (MSS) distribution at the four measurement stations is demonstrated in Fig. 6. Additionally for comparison, the measurements of the SFZ in measurement stations with the numerical results are presented in Table 5. The difference between the measured and calculated values is less than 10 %, therefore, the simulations are close to those measured by endoscopic measurements. Bearing in mind that the model does not simulate the overall complexity of the phenomenon (i.e., discontinuities in roof strata), it is considered to be a good approach despite the calculated SFZ is slightly smaller than the observed ones. Higher differences of about 15 % were observed in borehole 2-3. Underground tests showed that the fractured zones extend to 6.10 m, while numerical calculation indicated a value of 5.28 m, but it does not sound like that much when the actual difference is only 0.82 m. In comparison with Figs. 3 and 6, the numerical modeling does not catch fractures in borehole

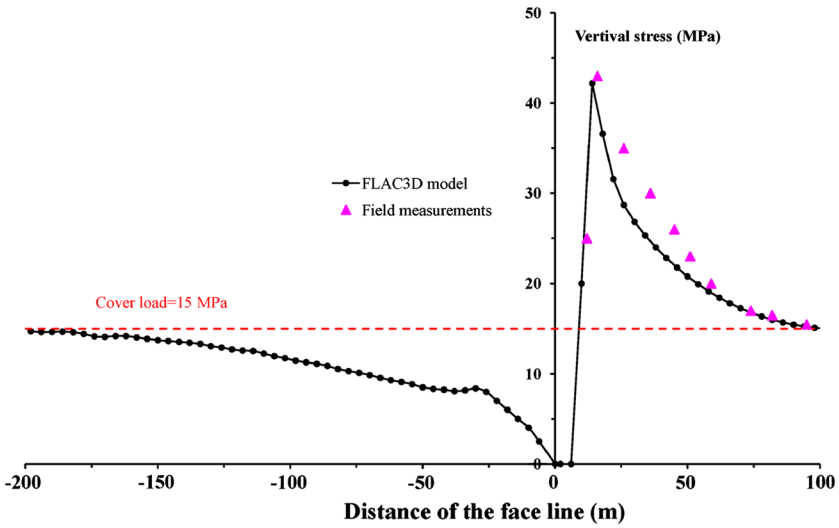

Fig. 5 Vertical stress along the longwall face by FLAC3D modeling and field measurements

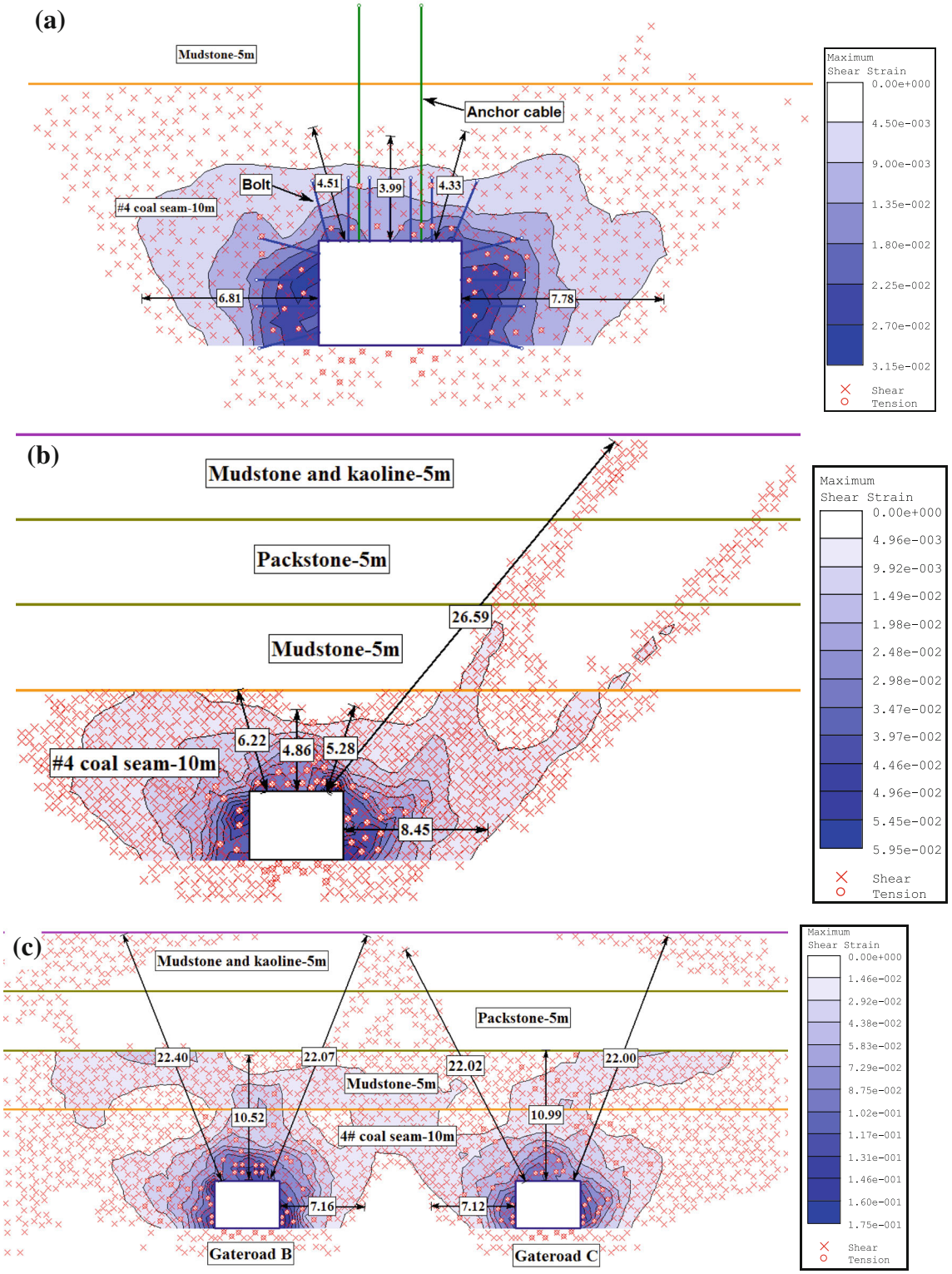

Fig. 6 Fracture and MSS distribution around gatetoads: **a** measurement station 1, **b** measurement station 2, **c** measurement station 3 and 4

3-3 and 4-3 where the boreholes through the 5 m thickness strong packstone, while the field measurement observed sparse fracture distribution in these areas. The reason for this deviation may be that the model used a continuum material, while the roof strata on-site contain various discontinuities.

Since measurement station 1 and 2 were in the same gateroad and had the similar geological conditions, the

Table 5 Comparison of the field measurements with numerical results

Station name	Borehole name	Distance from longwall face (m)	SFZ (m)		Difference between modeling and measurement	
			Measurement	Modeling	(m)	(%)
Station 1	1-1	70	4.58	4.51	−0.07	−1.55
	1-2		4.2	3.99	−0.21	−5.26
	1-3		4.6	4.33	−0.27	−6.24
	1-4		6.6	6.81	+0.21	+3.08
	1-5		7.8	7.78	−0.02	−0.26
Station 2	2-1	20	6.6	6.22	−0.38	−6.11
	2-2		5.0	4.86	−0.14	−2.88
	2-3		6.1	5.28	−0.82	−15.53
	2-4		8.7	8.45	−0.25	−2.96
Station 3	3-1	15	Choked	22.4	–	–
	3-2		11.1	10.52	−0.58	−5.51
	3-3		19.9	22.07	–	–
	3-4		7.1	7.16	+0.06	+0.084
Station 4	4-1	15	Choked	21.08	–	–
	4-2		11.6	10.99	−0.61	−5.55
	4-3		19.6	22.0	–	–
	4-4		7.9	7.12	−0.78	−10.96

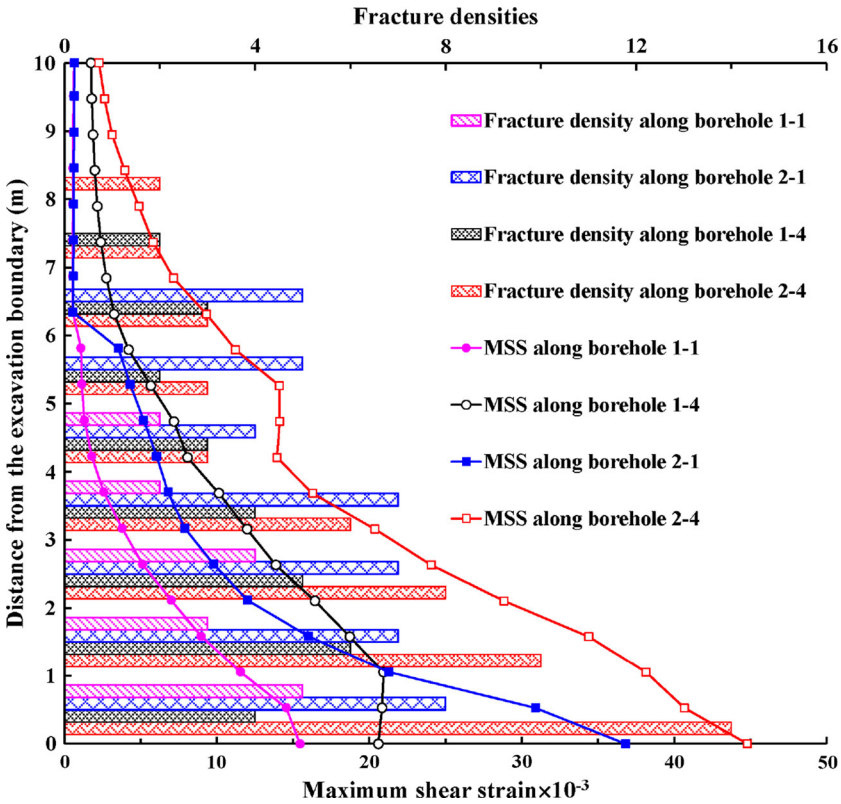

Fig. 7 Evolution of fracture densities and MSS in the observation holes in gateroad A as the longwall approaches, taking borehole 1-1 and 2-1, 1-4 and 2-4 for examples

observation results could be used to demonstrate the evolution of the SFZ and fracture density as the face approached. In comparison with Fig. 6a (70 m ahead of the face) and Fig. 6b (20 m ahead of the face), the SFZ increased as the face approached. Numerical modeling captured two shear bands in the upper strata at the panel side in

measurement station 2 (Fig. 6b). The main reason for this phenomenon can be that: measurement station 2 is close to the active face, and the surrounding roof strata bear relatively strong mining induced loading, resulting in shear dislocation in the upper strata at the panel side.

The numerical models also show that the shear stress plays a major role in the failure process, whereas tensile stress which is dominant close to the gateroads plays less of a role (Fig. 6). So the fracture densities (observed from the boreholes) and MSS (obtained from the numerical simulation) at measure station 1 (70 m ahead of the face) and measure station 2 (20 m ahead of the face) at the same borehole position were counted for comparison, as shown in Fig. 7, taking boreholes 1-1 and 2-1, 1-4 and 2-4 for examples. As the face approached, the fracture densities in boreholes 2-1 and 2-4 increased by 0–10 compared with those in boreholes 1-1 and 1-4. The closer the distance is from the gateroad boundary, the greater is the relative increase of fracture densities. The MSS performs the same variation tendency.

5 Discussion

Both field measurements and numerical simulations showed that the SFZ around the gateroads is significantly influenced by the abutment pressure due to longwall mining and the presence of bedding planes. As the face approaches, the fracture develops to deeper rock masses. The SFZ in the sidewalls in measurement station 2 is larger than that in measurement station 3 (Table 1). A reasonable explanation of this phenomenon is that gateroad C reliefs the stress concentration around gateroad B (Thomas 2010). Modeling results showed that the fractured zones in the coal pillar were linked in the upper part, while there was an arch-shaped non-fractured zone in the bottom part, as shown in Fig. 6c. Thus the coal pillar was unstable. However, few rib spallings had been found on the pillar, and a small convergence occurred in gateroad B and C. This indicates that, although the pillar had structurally failed, it is considered to be successful from a "functional" point of view (Esterhuizen et al. 2010). For the sake of safety, secondary reinforcement should be implemented in all of the three gateroads.

6 Conclusions

Field observations and numerical simulations were performed to characterize fracture distribution around gateroads under longwall influence in the Majialiang coalmine in Shuozhou city, Shanxi province, China. Overall, the observation results showed that the SFZ around the gateroad was dominated by longwall mining and strata bedding planes. As the longwall face approached, the front abutment pressure increased rapidly, and both SFZ and fracture densities increased in different degrees. The SFZ were about 8 m at the sidewalls, and more than 20 m in the roof at the place 20 m ahead the longwall face.

A 3D model combining with longwall gob simulation was carried out to determine the mining induced stresses around the gateroad, and detailed 2D models combined with the 3D stress results were used to capture the SFZ and MSS around the gateroad influenced by longwall mining. In general, significant agreements were achieved between field measurements and numerical results, and the MSS performed the same variation tendency. The numerical models also showed that the shear stress has a major role in the failure process, whereas tensile stress, which is dominant close to the gateroads, plays less of a role. Although investigations and modeling results showed that the total SFZ in the pillar was considerably large; it is a "functional" successful pillar in the field application. For the sake of safety, secondary reinforcement in the gateroads ought to be seriously considered, and the coal pillar design should be modified.

Acknowledgments Financial support for this work was provided by the Fundamental Research Funds for the Central Universities (2012LWB42), the Priority Academic Program Development of Jiangsu Higher Education Institutions (SZBF2011-6-B35).

References

Cai M (2008) Influence of stress path on tunnel excavation response-Numerical tool selection and modeling strategy. Tunn Undergr Space Technol 23(6):618–628

Chu BL, Hsu SC, Chang YL, Lin YS (2007) Mechanical behavior of a twin-tunnel in multi-layered formations. Tunn Undergr Space Technol 22(3):351–362

Coggan J, Gao FQ, Stead D, Elmo D (2012) Numerical modelling of the effects of weak immediate roof lithology on coal mine roadway stability. Int J Coal Geol 90:100–109

Dong FT, Song HW, Guo ZH, Lu SM, Liang SJ (1994) Roadway support theory based on broken rock zone. J China Coal Soc 19(1):21–33 (in Chinese)

Esterhuizen GS, Barczak TM (2006) Development of ground response curves for longwall tailgate support design. In: Proceedings of the 41st US symposium on rock mechanics, Colorado

Esterhuizen E, Mark C, Murphy MM (2010) Numerical model calibration for simulating coal pillars, gob and overburden response. In: Proceedings of the 29th international conference on ground control in mining, West Virginia, pp 44–57

Feng WK, Huang RQ, Li TB (2012) Deformation analysis of a soft-hard rock contact zone surrounding a tunnel. Tunn Undergr Space Technol 32:190–197

Hammah RE, Yacoub TE, Curran JH (2009) Probabilistic slope analysis with the finite element method. In: Proceedings of the 43rd US rock mechanics symposium and 4th US-Canada rock mechanics symposium, Asheville

Hao JH, Kang TH, Jin ZM, Zheng TB (2004) Similar simulation study on crack development law of surrounding rocks of roadway with great-thick thin-bedded top roof. Chin J Rock Mech Eng 23(19):3292–3297 (in Chinese)

Hoek E, Brown ET (1997) Practical estimates of rock mass strength. Int J Rock Mech Min Sci 34(8):1165–1186

Itasca Consulting Group Inc. (2006) FLAC3D (fast lagrangian analysis of continua in 3 dimensions), version 3.1 Software, Minneapolis, Minnesota, USA

Rocscience Inc. (2012) Phase V8 Software, Toronto, Ontario, Canada

Ryder JA, Wagner H (1978) 2D analysis of backfill as a means of reducing energy release rates at depth. Unpublished research report, Chamber of Mines of South Africa, Johannesburg

Thomas R (2010) The design and management of wide roadways in Australian coal mines. In: Proceedings of the 29th international conference on ground control in mining, West Virginia

Walentek A, Lubosik Z, Prusek S, Masny W (2009) Numerical model of the range of rock fracture zone around gateroads on the basis of underground measurement results. In: Proceedings of the 28th international conference on ground control in mining, West Virginia, pp 121–128

Wang C, Wang Y, Lu S (2000) Deformational behaviour of roadways in soft rocks in underground coal mines and principles for stability control. Int J Rock Mech Min Sci 37(6):937–946

Xie YS, Zhao YS (2009) Numerical simulation of the top coal caving process using the discrete element method. Int J Rock Mech Min Sci 46(6):983–991

Yavuz H (2004) An estimation method for cover pressure re-establishment distance and pressure distribution in the goaf of longwall coal mines. Int J Rock Mech Min Sci 41(2):193–205